**Structural, Spectroscopic, and Computational Evaluations of Cation-Cation and Halogen Bonding Interactions in Heterometallic Uranyl Hybrid Materials**

Korey P. Carter[ab], Mark Kalaj[ac], Sapphire McNeil[d], Andrew Kerridge[d], Mark H. Schofield[a], J. August Ridenour[a], and Christopher L. Cahill*[a]

[a] Department of Chemistry, The George Washington University, 800 22nd Street, NW, Washington, D.C. 20052, United States

[b] Chemical Sciences Division, Lawrence Berkeley National Laboratory, Berkeley, CA 94720, United States

[c] Department of Chemistry and Biochemistry, University of California, San Diego, La Jolla, CA 92093, United States

[d] Department of Chemistry, Lancaster University, Bailrigg, Lancaster LA1 4YB, United Kingdom

## Abstract

Harnessing the nominally terminal oxo atoms of the linear uranyl ($UO_2^{2+}$) cation represents a frontier within the field of f-element hybrid materials. Here we outline a route for systematically accessing uranyl oxo atoms via judicious pairing with $Ag^+$ cations or aryl iodo benzoic acids, and describe the syntheses and crystal structures of four new heterometallic compounds containing $Ag^+$ cations, the $UO_2^{2+}$ cation, and *o*- (**1**), *m*- (**2**), *p*-iodo- (**3**), and 2,5-diiodobenzoic acid (**4**) ligands. Vibrational and luminescence spectroscopic properties for all four compounds are reported, as are computational findings from quantum chemical calculations and density-based quantum theory of atoms in molecules (QTAIM) analyses. Single crystal X-ray diffraction analysis of compounds **1**-**4** shows that the nominally terminal uranyl oxo atoms are engaged in either covalent $UO_2$-Ag cation-cation interactions (CCIs) (**1** and **3**) or non-covalent assembly via halogen bonding interactions (**2** and **4**). Raman, infrared (IR), and luminescence spectra are redshifted with respect to the free uranyl cation indicating that both halogen-oxo and cation-cation interactions weaken the U=O bond, and in the case of compound **3** we note a rare example of activation of the uranyl asymmetric stretch ($\nu_3$) in the Raman spectra, likely due to the Ag-oxo CCI lowering the symmetry of the uranyl cation. Quantum chemical calculations and density-based quantum theory of atoms in molecules (QTAIM) analysis highlight a quantitative

difference between halogen bonds and CCIs, with the latter interactions shown to significantly decrease uranyl bond orders and electron density at bond critical points.

**Introduction**

The development of heterometallic uranyl hybrid materials is a topic of sustained interest as inclusion of a second metal in uranyl systems broadens the range of possible uranyl architectures and can lead to variation in material properties, such as luminescence, photochemistry, and magnetism, that are otherwise inaccessible in homometallic uranyl compounds.[1-12] The general approach for preparing heterometallic uranyl compounds relies upon the utilization of heterofunctional, multitopic ligands that feature multiple sites for potential metal-ligand coordination;[1, 6, 13, 14] however, inorganic crystal engineering, utilizing both supramolecular and coordination chemistry principles, offers additional levels of control in the hybrid material assembly process, and our group has previously demonstrated the ability to tune binding and non-covalent assembly in both the equatorial coordination sphere and at the uranyl oxo atoms.[15-19] Extending inorganic crystal engineering to heterometallic hybrid materials, wherein a fixed inorganic (uranyl) building block is paired with carefully selected organic ligand(s) and/or transition metal cation allows for investigation of structure-property trends in heterometallic uranyl hybrid materials and this approach is valuable as the means for tuning uranyl photophysical and vibrational properties have not been fully realized.

The utility of pairing $Ag^+$ with the uranyl cation to exploit $UO_2$-transition metal (TM) cation-cation interactions (CCIs) both structurally and spectroscopically has not been explored in detail and only a few examples of hybrid materials feature this mode of assembly.[2, 13, 20, 21] The redox-active $Ag^+$ presents a number of unique characteristics that make it an attractive choice as a secondary metal center in hybrid materials, including the ability to vary its bandgap depending

on coordination environment and the potential to turn on/off uranyl luminescence, which could lead to applications in photocatalysis.[2, 13, 22, 23] Moreover, $Ag^+$ is known for its ability to bind to both O and N, the common binding functionalities of most multitopic ligands, as well as its affinity for iodine, which we incorporate here via the use of iodobenzoate ligands. This latter pairing, between $Ag^+$ and I, is notable as $^{129}I$ is a problematic, gaseous fission product in nuclear waste processes, with $Ag^+$ based sorbents some of the most promising materials for $I_2$ capture during nuclear fuel reprocessing.[24, 25]

Herein we continue our work of pairing the uranyl cation with halogenated benzoic acids, as well as $Ag^+$ cations, and detail the synthesis of four novel compounds (**1**-**4**) with *o*-iodo-, *m*-iodo-, *p*-iodo, and 2,5-diiodobenzoic acid ligands. All compounds have been characterized via X-ray diffraction, vibrational and luminescence spectroscopy, and quantum chemical calculations, and structural analysis reveals that the aryl iodines of iodobenzoic acid ligands are not only supramolecular synthon sites, but also covalent bonding participants in heterometallic compounds.[26] Moreover, we observe that the nominally terminal uranyl oxo atoms are involved in either $UO_2$-Ag CCIs (**1** and **3**) or halogen bonding interactions (**2** and **4**), and thus this family of uranyl hybrid materials provides an excellent platform to structurally and spectroscopically evaluate these two assembly motifs, and uranyl oxo engagement more generally. Raman and luminescence spectroscopy are used to compare the two assembly motifs of **1**-**4**, and Raman spectra for all four compounds feature multiple $\nu_1$ bands ascribed to U–oxo bond symmetric stretching modes, with the lowest $\nu_1$ frequency noted for compound **3** (which also features the strongest CCI). We also observe activation of the uranyl asymmetric stretch ($\nu_3$) in the Raman spectra of **3**, which is quite unusual for a uranyl hybrid material. Luminescence spectra of **1**-**4** illustrate that while $UO_2$-Ag CCIs and halogen bonding interactions do influence resulting

spectra, the identity of the equatorial ligands also contribute to the observed evolution in photoluminescent behavior. Finally, quantum chemical calculations at the density functional (DFT) level of theory along with density-based quantum theory of atoms in molecules (QTAIM) analysis highlight quantitative differences in $UO_2$-Ag CCIs and halogen bonding interactions, with the former resulting in greater weakening of U-oxo bonds, which manifests as redshifts in vibrational and luminescence spectra.

## Experimental Section

### Materials and Methods

*Caution:* Whereas the uranium oxyacetate dihydrate $[UO_2(CH_3COO)_2]\bullet 2H_2O$ and uranyl nitrate hexahydrate $[UO_2(NO_3)_2]\bullet 6H_2O$ used in this study consists of depleted U, standard precautions for handling radioactive and toxic substances should be followed.

All organic materials, *o*-iodobenzoic acid (*o*-IBA) (Sigma-Aldrich, 98%), *m*-iodobenzoic acid (*m*-IBA) (Alfa Aesar, 98+%), *p*-iodobenzoic acid (*p*-IBA) (Sigma-Aldrich, 98%), and 2,5-diiodobenzoic acid (2,5-diIBA) (Sigma-Aldrich, 97%), were purchased and used as received. $AgNO_3$ (Alfa, 99.9+%) is also commercially available and was used without further modification.

### Synthesis

Compound **1**, $[UO_2Ag(C_7H_4IO_2)_2(NO_3)]_2$, was synthesized by combining $[UO_2(NO_3)_2]\bullet 6H_2O$ (0.124 g, 0.25 mmol), *o*-iodobenzoic acid (*o*-IBA) (0.126 g, 0.50 mmol), $AgNO_3$ (0.084 g, 0.50 mmol), sodium hydroxide (30 μL, 5M), and distilled water (3.0 g, 166.7 mmol) in a Parr autoclave (final pH 3.27) and then heating statically at 150 ºC for 48 hours. Upon removal from the oven, the sample was allowed to cool over four hours and the Parr autoclave was opened after approximately sixteen hours. Orange rectangular plate crystals were obtained from the bulk

product after decanting the supernatant liquor, washing three times with distilled water and ethanol, and air-drying at room temperature overnight.

Compounds **2**, $[UO_2Ag(C_7H_4IO_2)_3]_n$, **3**, $[UO_2Ag(C_7H_4IO_2)_3]_n$, and **4**, $[[UO_2Ag(C_7H_3I_2O_2)_3]_n]_2$, were prepared following the same procedure as **1** with *m*-iodo- (*m*-IBA) (0.126 g, 0.50 mmol), *p*-iodo- (*p*-IBA) (0.126 g, 0.50 mmol), and 2,5-diiodobenzoic acid (2,5-diIBA) (0.126 g, 0.50 mmol) replacing *o*-IBA in **2**-**4**, respectively. Additionally, for **3**, $[UO_2(NO_3)_2]\bullet 6H_2O$ was replaced by $[UO_2(CH_3COO)_2]\bullet 2H_2O$ (0.105 g, 0.25 mmol). Final pH values for **2**-**4** were 3.36, 3.73, and 3.51, respectively. Upon cooling to room temperature and washing with distilled water and ethanol, X-ray quality orange plate crystals were separated from the bulk product for all three materials.

**Characterization**

**X-Ray Structure Determination**

Single crystals from each bulk sample were isolated and mounted on MiTeGen micromounts. Structure determination for each of the single crystals was achieved by collecting reflections using 0.5˚ ω scans on a Bruker SMART diffractometer equipped with an APEX II CCD detector using MoKα (λ=0.71073 Å) radiation at 293(2) K. The data were integrated using the SAINT software package[27] contained within the APEX II software suite[28] and absorption corrections were applied using *SADABS*.[29] The crystal selected from the bulk product of compound **4** was a two component non-merohedral twin that was accounted for using *TWINABS*.[30] Compound **1** was solved via the Patterson Method (SHELXS-2014),[31] whereas **2**-**4** were solved via direct methods using SIR 92,[32] and all four compounds were refined using SHELXL-2014[31] contained within the WinGX[33] software suite. In each structure, all non-hydrogen atoms were located via difference Fourier maps and refined anisotropically. Aromatic hydrogen atoms were located via

difference Fourier maps, yet were placed at their idealized positions and allowed to ride on the coordinates of their parent carbon atom (($U_{iso}$) fixed at $1.2U_{eq}$). All figures were prepared with Crystal Maker,[34] and data collection and refinement details for **1**-**4** are included in Table 1.

**Table 1** Crystallographic Data for Compounds **1**-**4**

| | **1** | **2** | **3** | **4** |
|---|---|---|---|---|
| chem formula | $C_{28}H_{16}I_4N_2O_{18}Ag_2U_2$ | $C_{21}H_{12}I_3O_8AgU$ | $C_{21}H_{12}I_3O_8AgU$ | $C_{21}H_9I_6O_8AgU$ |
| formula weight | 1867.83 | 1118.91 | 1118.91 | 1496.58 |
| crystal system | triclinic | triclinic | monoclinic | triclinic |
| space group | P-1 | P-1 | $P2_1/n$ | P-1 |
| $a$ (Å) | 8.8109(4) | 8.677(7) | 9.1545(5) | 11.210(7) |
| $b$ (Å) | 11.4713(6) | 9.815(8) | 14.2946(7) | 12.407(8) |
| $c$ (Å) | 11.4852(6) | 15.0560(11) | 19.4243(10) | 23.0870(11) |
| $\alpha$ (deg) | 117.072(4) | 97.859(6) | 90 | 77.655(6) |
| $\beta$ (deg) | 106.043(3) | 98.971(7) | 93.878(11) | 82.316(6) |
| $\gamma$ (deg) | 91.445(3) | 101.625(7) | 90 | 74.954(7) |
| $V$ (Å$^3$) | 977.81(9) | 1221.7(14) | 2536.0(2) | 3019.0(3) |
| $Z$ | 1 | 2 | 4 | 4 |
| $T$ (K) | 293(2) | 293(2) | 293(2) | 293(2) |
| $\lambda$ (Mo K$\alpha$) | 0.71073 | 0.71073 | 0.71073 | 0.71073 |
| $D_{calc}$ (g cm$^{-3}$) | 3.172 | 3.042 | 2.931 | 3.293 |
| $\mu$ (mm$^{-1}$) | 12.476 | 11.256 | 10.845 | 12.183 |
| $R_{int}$ | 0.0297 | 0.0662 | 0.0421 | 0.0332 |
| R1 [$I>2\sigma(I)$] | 0.0384 | 0.0419 | 0.0297 | 0.0387 |

| | | | | |
|---|---|---|---|---|
| wR2 [$I>2\sigma(I)$] | 0.0879 | 0.0821 | 0.0720 | 0.0849 |

**Powder X-ray Diffraction**

Powder X-ray diffraction (PXRD) data on the bulk reaction product of compounds **1**-**4** (Figures S4-S7, Supporting Information) were used to examine the purity of each sample. All data were collected on a Rigaku Miniflex (Cu Kα, 2θ=3-60˚) and were analyzed using the Match software program.[35] Initially, the bulk products of compounds **1**, **3**, and **4** were found to contain multiple solid-state phases. The impurity for **1** was removed by not including any NaOH in the reaction vessel during synthesis (lowering the final pH to 2.31), while minor impurities persisted in the bulk products of **3** and **4** upon synthesis using a range of conditions and upon washing with a wide array of organic solvents. As a result, single crystals of **3** and **4** were hand-selected for all spectroscopic characterization described herein.

**Spectroscopic Characterization**

Infrared spectra of single crystals of **1**-**4** were collected using a Bruker Tensor 27 FT-IR microspectrometer. Crystals were placed on glass microscope slides at room temperature and crushed using a diamond attenuated total reflectance (ATR) microscope objective with a beam aperature of 100 μm, over the range 400 to 4000 $cm^{-1}$.

Raman spectra for single crystals of **1**-**4** were collected using a Bruker Sentinel system equipped with a 785 nm 400 mW laser and a high sensitivity TE-cooled, 1024 x 255 CCD array linked via fiber optics to a video assisted Raman probe in a microscope mount. The spectra were collected for fifteen seconds with four signal accumulations over the range of 80-3200 $cm^{-1}$.

Room temperature, solid-state luminescence measurements were obtained for **1**-**4** on a Horiba JobinYvon Fluorolog-3 spectrophotometer. Data were manipulated using the FluoroEssence

software package and experimental parameters (slit width, integration time, etc.) were adjusted on a sample-by-sample basis to obtain suitable data with a sufficiently high signal-to-noise ratio.

**Computational Details**

Density functional theory (DFT) was used to calculate partially optimized structures and vibrational frequencies for **1-4**, and was initially carried out using the hybrid-GGA B3LYP exchange-correlation functional, which has been shown to reproduce experimental parameters of uranyl complexes with high accuracy.[36, 37] The Dunning aug-cc-pVDZ basis set[38] was used for all atoms except I, Ag, and U, for which Ahlrichs def-SVP basis set and accompanying effective core potentials (ECPs) were used.[39] For greater context, additional DFT calculations at the B3LYP level were run, which utilized the ECP60MWB and ECP60MWB_SEG basis sets for U,[40-42] the def2-TZVP basis set for C, H, N, and O,[39] and ECPs for Ag[43] and I.[44] Calculations were performed using either the Turbomole quantum chemistry software suite (v 7.3)[45] or Gaussian16[46] in combination with NBO7.[47, 48] Analysis of resultant electron densities was performed in the AIMA11 software suite[49] using Bader's Quantum Theory of Atoms in Molecules (QTAIM) approach.[50] Visualizations of calculated results were generated with GaussView 6[51] or Avogadro.[52]

**Results**

**Description of Structures**

Single crystal X-ray crystallographic analyses revealed that each of the four compounds in this family of materials feature unique local structures about the uranyl and silver metal centers. Additionally, modes of connectivity and/or supramolecular assembly vary for all compounds, thus they are described in detail for **1-4** as well.

Compound **1**, $[UO_2Ag(C_7H_4IO_2)_2(NO_3)]_2$, is a $UO_2$-Ag heterometallic material featuring *o*-IBA ligands that crystallizes in the space group P-1. The single crystallographically unique $[UO_2]^{2+}$ cation adopts hexagonal bipyramidal geometry and features two bidentate *o*-IBA ligands in the equatorial plane along with a bidentate nitrate group (bound via O5 and O6) (Figure 1). U1-O bonds to the two bidentate *o*-IBA ligands (O3, O4, O7, O8) are at an average distance of 2.446 Å, whereas U1-O distances to the bidentate nitrate group are 2.485(6) Å (U1-O5) and 2.482(6) Å, respectively. The local structure of **1** also features a five-coordinate silver cation (Ag1) which adopts square pyramidal molecular geometry and binds to two carboxylate oxygen atoms (O3, O8), two aryl iodines from *o*-IBA ligands (I1, I2), and a uranyl oxo atom (O2) on the symmetry equivalent $[UO_2]^{2+}$ cation to generate a binuclear secondary building unit (SBU) (Figure 1). Forming the base of the Ag square pyramid are Ag1-O (carboxylate) bonds at distances of 2.403(6) Å (Ag1-O3) and 2.500(6) Å (Ag1-O8), respectively, and Ag1-I bonds at distances of 2.7213(10) Å (Ag1-I1) and 2.6848(10) Å (Ag1-I2). The Ag1-O2 CCI in **1** is at the apex of the Ag pentagonal bipyramid at a distance of 2.464(7) Å, and this is the first of two occurrences of this bonding motif we describe herein. O2 participation in the CCI *does not* seem to alter the U=O bond significantly as U-oxo bond lengths are statistically equivalent at 1.746(7) Å (U1-O1) and 1.743(7) Å, respectively.

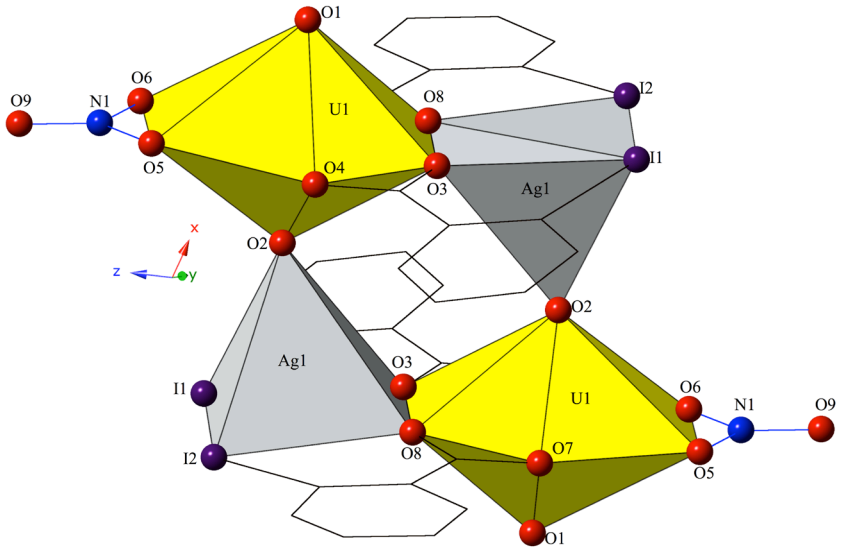


**Figure 1** Polyhedral representation of compound **1** highlighting local coordination environments of $UO_2^{2+}$ and $Ag^+$ cations. Yellow polyhedra are U(VI) centers and silver polyhedra are Ag(I) centers, whereas red spheres are oxygen atoms, purple spheres are iodine atoms, and blue spheres are nitrogen atoms. All H atoms have been omitted for clarity.

The heterometallic dimers of **1** are assembled into a supramolecular 1D chain along the [001] direction via halogen bonding interactions between an *o*-IBA iodine atom (I2) from one SBU with an oxygen atom (O9) from the nitrate moiety on the neighboring SBU (Figure 2), and the corresponding I-O interaction distance and angle are 3.331(7) Å (95.2% sum of the van der Waals radii) and ∠C-I•••O 162.7(7)º.

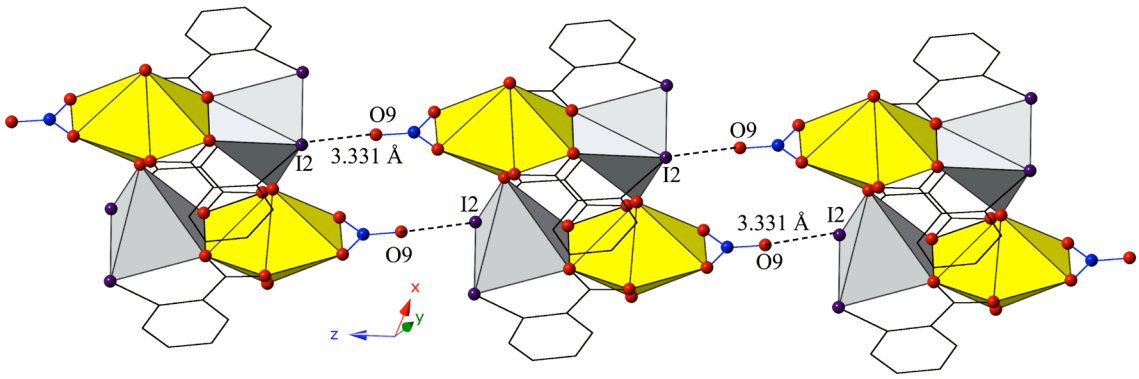


**Figure 2** Compound **1** viewed along the [001] direction highlighting halogen bonding interactions that link heterometallic dimers of **1** into a 1D chain.

Switching from *o*-IBA to *m*-IBA yields compound **2**, $[UO_2Ag(C_7H_4IO_2)_3]_n$, which crystallizes in the space group P-1. Similar to **1**, the single crystallographically unique $[UO_2]^{2+}$ cation adopts hexagonal bipyramidal geometry, yet in **2**, equatorial coordination is exclusively bidentate *m*-IBA ligands, and U1-O bond distances to the three *m*-IBA ligands (O3-O8) are at an average of 2.472 Å (Figure 3). The structure of **2** also features a four-coordinate silver cation (Ag1) that adopts distorted tetrahedral molecular geometry and binds to two carboxylate oxygen atoms (O4, O5) and two aryl iodines from *m*-IBA ligands (I1, I3) (Figure 3). Ag1-O (carboxylate) bonds are at distances of 2.413(6) Å (Ag1-O4) and 2.339(6) Å (Ag1-O5), whereas Ag1-I bonds are at distances of 2.9750(15) Å (Ag1-I1) and 2.820(2) Å (Ag1-I3).

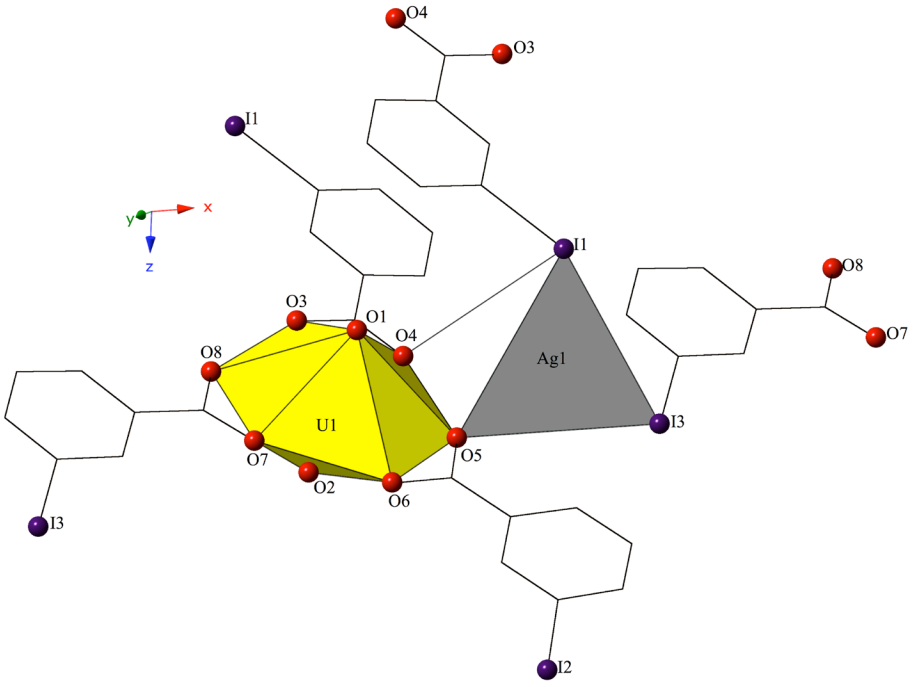


**Figure 3** Polyhedral representation of compound **2** detailing local coordination environments of $UO_2^{2+}$ and $Ag^+$ cations. All H atoms have been omitted for clarity.

The mononuclear $UO_2$-Ag SBUs highlighted in Figure 3 are linked to form a 1D chain along the [100] direction via the two Ag-I bonds described above, and the chains of **2** are further assembled into a supramolecular 2D sheet in the (010) plane via halogen bonding interactions

between an *m*-IBA iodine atom (I3) from one SBU with a uranyl oxo atom (O2) on the neighboring SBU (Figure 4). The corresponding I-O interaction distance and angle are 3.415(7) Å (97.6% sum of the van der Waals radii) and ∠C-I•••O 127.5(3)º, and these interactions in **2** mark the first of two examples of this assembly motif observed in this family of compounds. We also note that oxo atom (O2) participation in the halogen bonding interactions of **2** *does* result in small differences in U=O bond lengths as the U1-O2 bond distance is 1.768(6) Å, whereas the U1-O1 bond is at a distance of 1.746(6) Å.

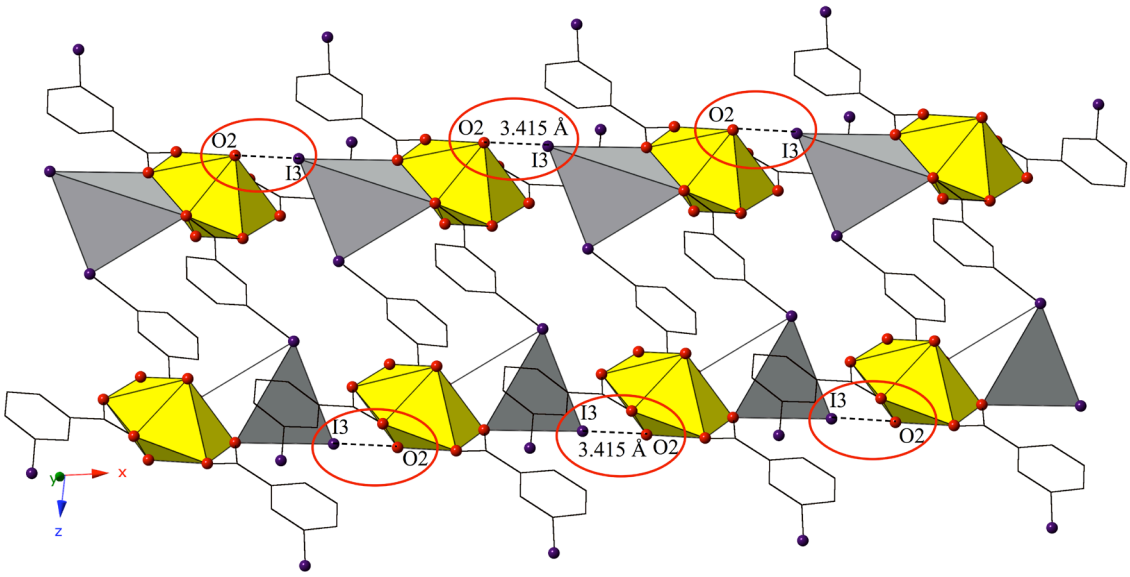


**Figure 4** Supramolecular 2D sheet of compound **2** viewed in the (010) plane. Halogen bonding interactions with uranyl oxo atoms that link 1D chains of **2** to form a 2D sheet are highlighted in red circles.

The introduction of *p*-IBA yields compound **3**, $[UO_2Ag(C_7H_4IO_2)_3]_n$, which crystallizes in the space group $P2_1/n$. The single crystallographically unique $[UO_2]^{2+}$ cation adopts hexagonal bipyramidal geometry, and similar to **2**, equatorial coordination is exclusively bidentate IBA ligands (in this case *p*-IBA) with U1-O bond distances to the three *p*-IBA ligands (O3-O8) at an average of 2.453 Å (Figure 5). The local structure of **3** also features a four-coordinate silver

cation (Ag1) which adopts tetrahedral molecular geometry and links three uranyl centers via coordination to two carboxylate oxygen atoms (O6, O7), an aryl iodine atom from a *p*-IBA ligand on a neighboring unit (I1), and a uranyl oxo atom (O1) on another symmetry equivalent $[UO_2]^{2+}$ cation to generate a trinuclear SBU (Figure 5). Forming the base of the Ag tetrahedron are Ag1-O (carboxylate) bonds at distances of 2.397(4) Å (Ag1-O6) and 2.375(4) Å (Ag1-O7), respectively, and the Ag1-O2 CCI at a distance of 2.343(4) Å. Completing the Ag tetrahedron in **3** is the Ag1-I1 bond, which forms the apex of the tetrahedron, and is at distance of 2.700(7) Å. In contrast to **1** where we noted U=O bond lengths did not vary with oxo atom participation in a $UO_2$-Ag CCI, we do observe small changes in the U=O bond lengths of **3** which are at distances of 1.772(4) Å (U1-O1) and 1.793(4) Å, respectively.

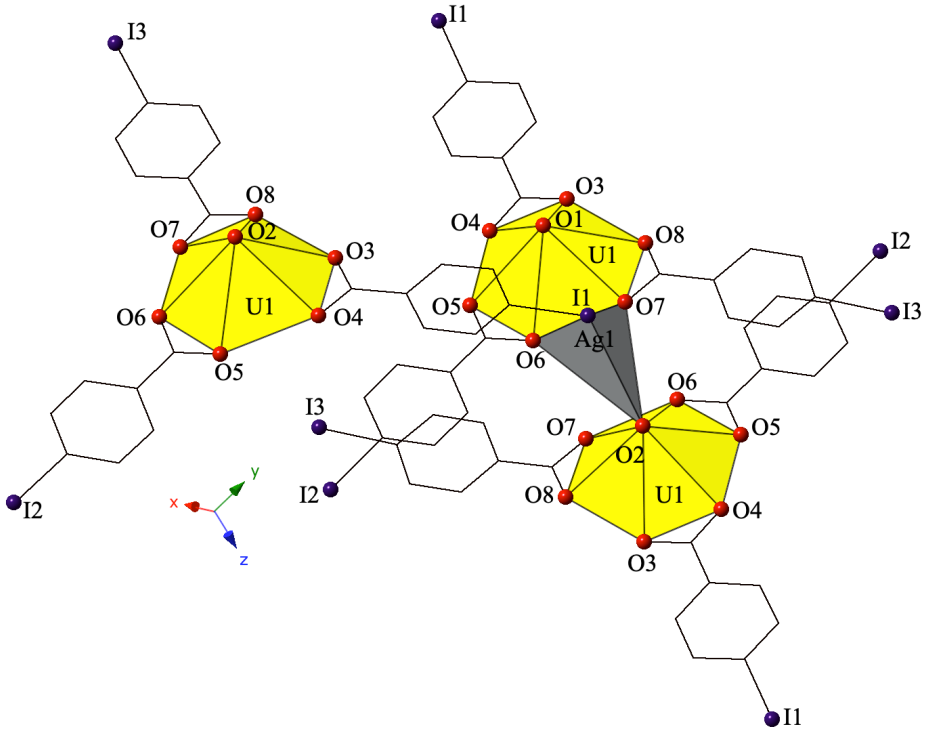


**Figure 5** Polyhedral representation of compound **3** detailing local coordination environments of $UO_2^{2+}$ and $Ag^{+}$ cations. All H atoms have been omitted for clarity.

The trinuclear $UO_2$-Ag SBUs highlighted in Figure 5 are linked to form a 2D sheet in (100) plane via the combination of Ag-O and Ag-I bonding along with $UO_2$-Ag CCIs described above (Figure 6). Supplementing the formation of sheets are bifurcated halogen bonding interactions between an iodine from one *p*-IBA ligand (I3) and two carboxylate oxygen atoms (O4, O5) on a neighboring SBU (Figure 6). The bifurcated linkage features an iodine atom (I3) acting as a halogen bond donor, and the halogen bonding interactions with carboxylate oxygen atoms are at distances of 3.413(4) Å (I3-O4) (97.5% sum of the van der Waals radii) and 3.342(4) Å (I3-O5) (95.5% sum of the van der Waals radii), respectively, with corresponding angles of ∠C19-I3•••O4 153.54(17)º and ∠C19-I3•••O5 157.74(17)º.

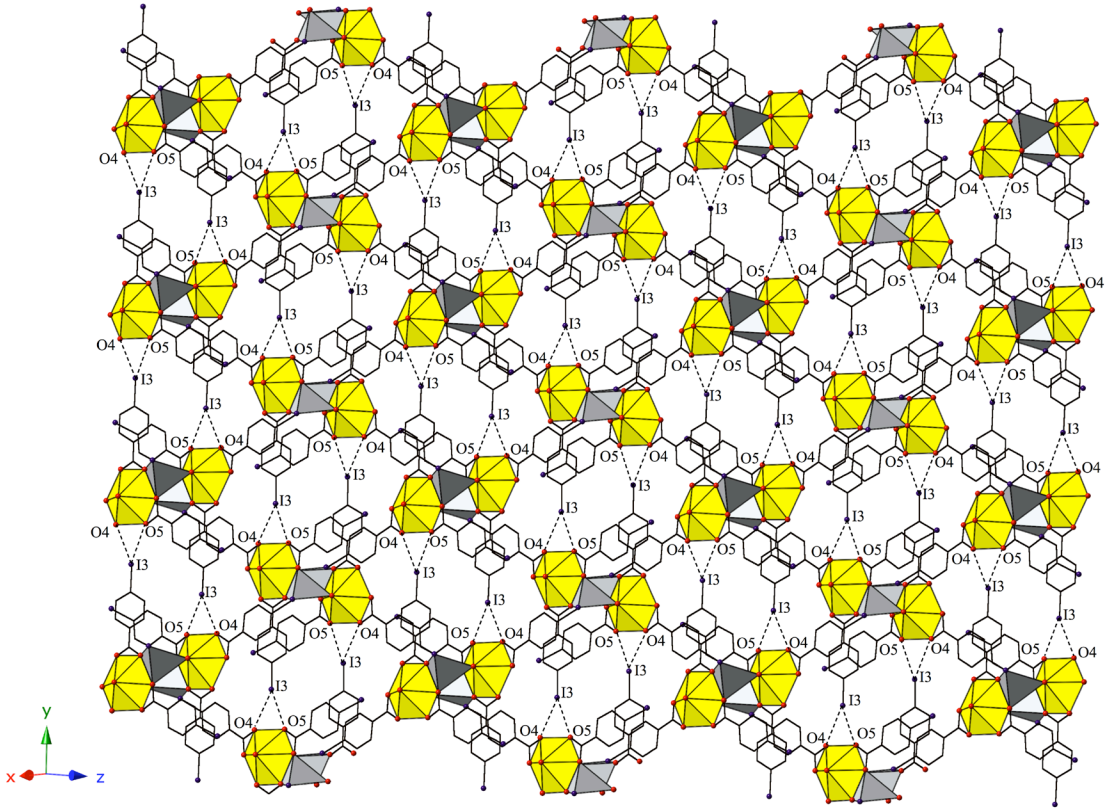


**Figure 6** 2D sheet of compound **3** viewed in the (100) plane. Bifurcated halogen bonding interactions with carboxylate oxygen atoms that supplement formation of sheets of **3** are shown.

Switching from the mono-substituted *p*-IBA to 2,5-diIBA resulted in compound **4**, $[[UO_2Ag(C_7H_3I_2O_2)_3]_n]_2$, which crystallizes in the space group P-1. Compound **4** features two crystallographically unique $[UO_2]^{2+}$ cations, both of which adopt hexagonal bipyramidal geometries. Both $[UO_2]^{2+}$ cations feature equatorial coordination to three 2,5-diIBA ligands and the average U1-O (O5-O10) bond distance is 2.469 Å, whereas the average U2-O (O11-O16) bond distance is 2.467 Å (Figure 7). The local structure around both uranyl cations in **4** also features five-coordinate silver cations (Ag1, Ag2), which each adopt distorted trigonal bipyramidal molecular geometries as a result of coordination to two carboxylate oxygen atoms and three aryl iodine atoms, respectively, from 2,5-diIBA ligands (Figure 7). Ag1-O(carboxylate) bond distances are 2.368(5) Å (Ag1-O8) and 2.632(6) (Ag1-O9), whereas Ag2-O(carboxylate) bonds are at distances of 2.375(5) Å (Ag2-O11) and 2.594(5) Å (Ag2-O14). Ag-I bond distances are at averages of 2.843 Å for Ag1 (I1, I3, I5) and 2.848 Å for Ag2 (I7, I9, I11), and Ag coordination via the different sites (O and I) on the 2,5-diIBA ligands yields two identical, yet crystallographically unique mononuclear SBUs.

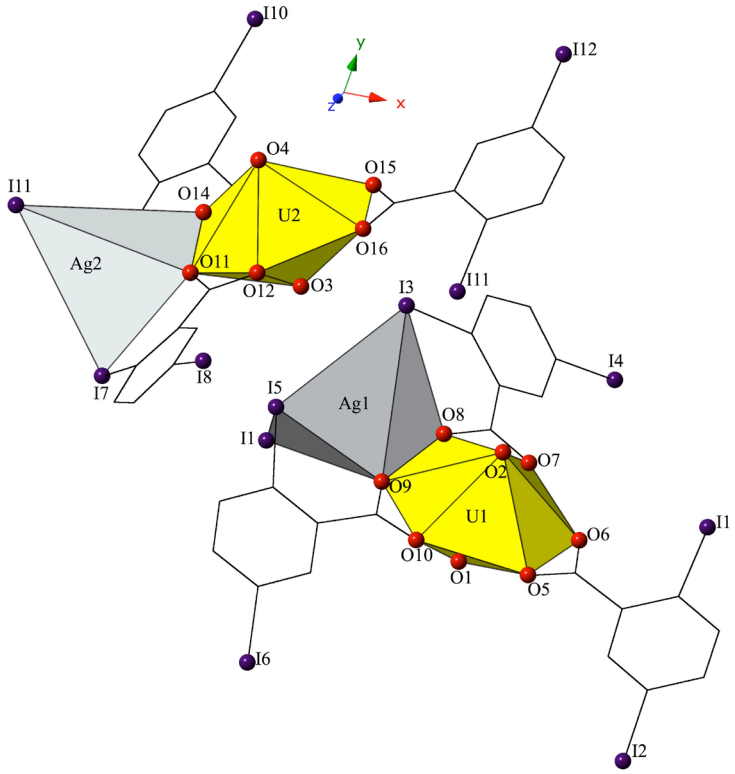


**Figure 7** Polyhedral representation of compound **4** detailing local coordination environments of the two crystallographically unique $UO_2^{2+}$ and $Ag^+$ cations. All H atoms have been omitted for clarity.

The two unique SBUs of **4** shown in Figure 7 are linked to form two, parallel 1D chains along the [100] direction via the Ag-O and Ag-I bonds described previously (Figure 8). Additional assembly of the chains of **4** into supramolecular 2D sheets occurs via two distinct bifurcated halogen bonding interactions with uranyl oxo atoms on the neighboring chains (Figure 8). The bifurcated interactions are between uranyl oxo atoms (O2 and O3) and iodine atoms from four unique 2,5-diIBA ligands (I3, I5, I7, I9), all of which are also participating in bonding with Ag cations. The first of two interactions is between uranyl oxo atom (O2), acting here as a halogen bond acceptor, and the iodine atoms I7 and I9 and the corresponding interaction distances and angles are 3.376(5) Å (I2-O7) (96.5% sum of the van der Waals radii), 3.047(5) Å (I2-O9) (87.1% sum of the van der Waals radii), ∠C24-I7•••O2 167.4 (2)º, and ∠C31-I9•••O2

174.3(3)º (Figure 8, blue boxes). The second, unique bifurcated interactions is between the uranyl oxo atom (O3), also acting as a halogen bond acceptor, and the iodine atoms I3 and I5 with interaction distances of 3.182(5) Å (I3-O3) (90.9% sum of the van der Waals radii) and 3.078(5) Å (I3-O5) (87.9% sum of the van der Waals radii), respectively, and corresponding angles of ∠C10-I3•••O3 169.5(2)º and ∠C17-I5•••O3 168.4(2)º (Figure 8, red boxes). Similar to **2**, we *do* note that oxo atom (O2, O3) participation in the halogen bonding interactions of **4** does result in small differences in U=O bond lengths as the U1-O2 and U2-O3 bond distances are 1.777(5) Å (U1-O2) and 1.776(5) Å (U2-O3), respectively, whereas the U1-O1 and U2-O4 bonds are at distances of 1.747(6) Å and 1.750(6) Å.

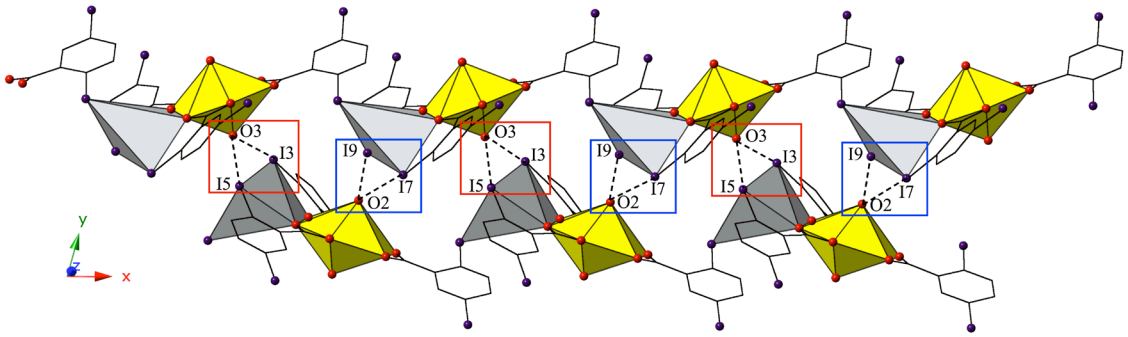


**Figure 8** Unique chains of compound **4** viewed in the (001) plane. Bifurcated halogen bonding interactions with uranyl oxo atoms that link chains to form supramolecular 2D sheets are highlighted in blue and red boxes.

**Structural Discussion**

As compounds **1-4** were synthesized from similar reaction conditions, the resulting structures provide an opportunity to assess the impact of including $Ag^{+}$ as a secondary metal center in uranyl hybrid materials on means of covalent and non-covalent assembly. The equatorial environments about the uranyl cations of **1-4** are nearly identical (bidentate carboxylate coordination), the nitrate group in **1** is the only anomaly, thus we can attribute the

observed modulations in hybrid material dimensionality and evolution of modes of assembly to the $Ag^+$ secondary metal centers, and to a lesser extent to changes in aryl iodine position about the benzoic acid ligands. Of particular note in **1**-**4**, the nominally terminal uranyl oxo atoms are involved in either $UO_2$-Ag CCIs (**1** and **3**) or halogen bonding interactions (**2** and **4**), thus this family of uranyl hybrid materials also provides a unique platform to evaluate these two synthons involving uranyl oxo atoms (Table 2).

**Table 2** Summary of Uranyl Oxo Participation in Covalent and Non-Covalent Assembly in Heterometallic $UO_2$-Ag Compounds **1**-**4**.

| Compound | Benzoic Acid Ligand | Dimensionality | $UO_2$-Ag CCI | Halogen Bonding with Oxo Atoms |
|---|---|---|---|---|
| **1** | *o*-IBA | Molecular | Yes | No |
| **2** | *m*-IBA | 1D Chain | No | Yes |
| **3** | *p*-IBA | 2D Sheet | Yes | No |
| **4** | 25diIBA | 1D Chains (x2) | No | Yes (x4) |

Compounds **1-4** feature uranyl cations coordinated by iodo-functionalized benzoic acid ligands (*o-, m-, p*-IBA, and 2,5-diIBA) to form anionic units, which are charge balanced and further coordinated by $Ag^+$ secondary metal centers to form heterometallic SBUs. In compound **1** (with *o*-IBA), we observe a square pyramidal, five-coordinate Ag(I) cation which participates in a $UO_2$-Ag CCI. This interaction links uranyl units to form a heterometallic molecular dimer at a distance of 2.464(7) Å, which is indicative of genuine Ag-oxo bonding as the interaction distance is at 76.0% the sum of the van der Waals radii. $UO_2$-Ag CCIs are relatively rare in the hybrid material literature, and the examples in **1** (and **3**) are only the third and fourth examples of this bonding motif in heterometallic $UO_2$-Ag carboxylate compounds.[21, 53] In compound **2** (with *m*-

IBA), we note a distorted tetragonal, four-coordinate Ag(I) cation, which binds two carboxylate oxygens and two aryl iodines in the uranyl equatorial plane. Instead of a $UO_2$-Ag CCI (in a molecular compound), we observe a uranyl coordination polymer where uranyl oxo atom participation in halogen bonding interactions supplements covalent metal-to-ligand assembly. Whereas halogen bonding with the uranyl oxo atoms remains relatively unusual, it can be a robust supramolecular synthon, in particular with iodine atoms, as our group has demonstrated in multiple recent studies.[15, 16, 19, 54-56] In compound **3** (with *p*-IBA), we observe a tetragonal, four-coordinate Ag(I) cation which once again participates in a $UO_2$-Ag CCI. The CCI links uranyl units to form a heterometallic trinuclear SBU at a distance of 2.343(4) Å, which is the shortest bond distance ever observed in a $UO_2$-Ag CCI,[13, 53] and these SBUs are further linked to form 2D sheets. Bifurcated halogen bonding interactions supplement sheet formation in **3**, yet unlike **2**, do not involve the uranyl oxo atoms. In compound **4** (with 2,5-diIBA), we note two crystallographically unique distorted trigonal bipyramidal, five-coordinate Ag(I) cations, which each bind two carboxylate oxygens and three aryl iodines in the uranyl equatorial plane. The Ag-O and Ag-I coordination from the two Ag(I) cations links heterometallic SBUs to form two, parallel 1D chains, which are further assembled into 2D sheets via bifurcated halogen bonding interactions with uranyl oxo atoms. This is an interaction motif that has been observed once before in a uranyl hybrid material,[55] yet the 'strengths' of the interactions in **4** are notable (three of four I-oxo interactions at <91% sum of the van der Waals radii).

Looking at the dimensionality and means of assembly observed in **1**-**4**, and the electronic manifestations thereof, we can make two comments about the role of the $Ag^+$ as a secondary metal center. In terms of modulating uranyl hybrid material dimensionality, we do not see the silver cation play a significant role in **1**-**4**. Uranyl hybrid materials are known to form 1D and 2D

planar architectures,[3, 4] and this is what was observed in **1-4**; however, regarding *modes* of assembly, specifically those involving the nominally terminal uranyl oxo atoms, we do note that $Ag^+$ inclusion in the hybrid materials seems to exert some influence. Moreover, the character of U=O bonds can be impacted by changing the extent to which electron density is donated to the uranyl unit.[36, 57] The consistent presence of silver in the equatorial plane, via coordination with carboxylate oxygen atoms, would likely contribute additional electron density to the uranyl unit, thereby weakening the U=O bonds, and making them 'better' interaction acceptors. Compounds **1-4** experimentally verify this prediction with all materials featuring either robust $UO_2$-Ag CCIs (**1** and **3**) or strong halogen bonding interactions (**2** and **4**), and computational details on the nature and strength of the CCIs and halogen bonds are detailed below.

**Vibrational and Luminescence Spectroscopy**

Raman and infrared (IR) spectroscopy are complementary spectroscopic methods which reveal information regarding bonding and local environments for uranyl compounds and species.[58] The uranyl cation is known to feature three characteristic vibrational modes and the symmetric ($\nu_1$, 860-880 $cm^{-1}$, Raman active) and asymmetric ($\nu_3$, 930-960 $cm^{-1}$, infrared active) stretching modes are known to be sensitive to coordinating ligands, a direct result of uranyl bond weakening due to ligand coordination in equatorial plane.[58-60] Uranyl stretching modes are also often used as diagnostics of ionic/covalent bonding and non-covalent interaction strength as well as probes of equatorial covalency.[61] Recently we quantified equatorial coordination and oxo interaction contributions to uranyl vibrational spectra in a series of homometallic compounds,[54] and here we aim to extend these efforts to heterometallic species while also delineating spectroscopic differences between CCIs and halogen bonding interactions at uranyl oxo atoms.

Looking at the Raman spectra of compounds **1**-**4**, which are highlighted in Figure 9, we note multiple peaks in the spectral window where we expect the uranyl symmetric stretch ($\nu_1$). This is a likely result of the Ag-oxo bonding and halogen-oxo interactions at the uranyl moiety in **1**-**4**, which may lower the idealized $D_{\infty h}$ point group symmetry of the $[UO_2]^{2+}$ unit. Distortion of the uranyl cation or a change in the local point group symmetry can result in the removal of degeneracy and thus Raman activation of the asymmetric $\nu_3$ mode and infrared activation of the symmetric $\nu_1$ mode are both possible.[58] The likely reason for observation of multiple peaks in the area of the symmetric stretching vibrational mode ($\nu_1$) in Figure 9 lies in the crystal structures of these compounds where the $UO_2$-Ag CCIs and I-oxo halogen bonding interactions in **1**-**4** lower the symmetry of the sites occupied by U atoms in the crystals, resulting in the splitting of degenerate modes and activation of modes otherwise inactive in the Raman or IR spectra. As a result, Raman spectra can show multiple $\nu_1$ bands ascribed to each of the U–oxo bond symmetric stretching modes, and this is what is noted in Figure 9.

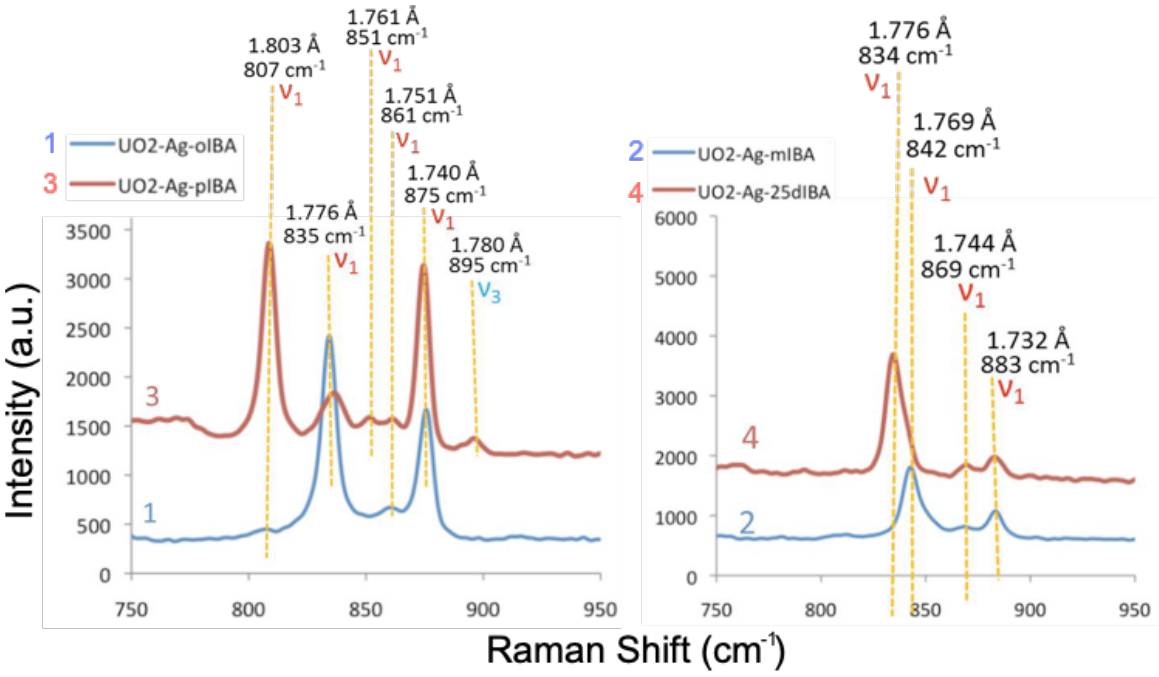


**Figure 9** Identification of the Raman peaks of **1**-**4** and calculated corresponding U-oxo bond lengths. $\nu_1$ and $\nu_3$ indicate peaks correspond to the symmetric and asymmetric stretches of the uranyl cation, respectively.

The Raman spectra of **1**-**4** also allow us to take a closer look at the effects of $UO_2$-Ag CCIs and halogen bonding at the uranyl oxo groups. An oxo linkage between the uranyl moiety and a silver cation or a halogen bond at the uranyl oxo atoms could lead to a decrease in the strength and increase in the length of the U–oxo bond. The closer an $Ag^+$ cation is to the oxo group, the larger the influence is expected to be on the bond lengths according to Badger's Rule,[62, 63] and the Raman spectra of compounds **1** and **3** are consistent with this empirical expectation. The shortest Ag-oxo CCI is observed in **3**, at 2.343(4) Å, and it is in the spectra of **3** where we observe the most peaks in the window of interest, including one of the lowest $\nu_1$ frequencies observed in a uranyl compound (807 $cm^{-1}$).[58] Additionally, we note a small peak at 895 $cm^{-1}$, which we attribute to activation of the uranyl asymmetric stretch in the Raman spectra (Figure 9). This is indicative of the Ag-oxo CCI in **3** lowering the symmetry of the uranyl cation

to something other than $D_{\infty h}$, and one explanation for the bond length and interaction distance variations in **1**-**4**, and in compound **3** in particular, is 'charge transfer' from $Ag^{+}$ cations or iodine atoms to the central uranium atom of the uranyl moiety, which would weaken the U-oxo bonds and result in bond elongation.

To further investigate possible CCI or halogen bond mediated charge transfer we looked at the photoluminescence of compounds **1**-**4**. Uranyl materials are known to exhibit a characteristic green emission profile that results from ligand-to-metal charge transfer transitions between uranyl bonding ($3\sigma_u$, $3\sigma_g$, $2\pi_u$, and $1\pi_g$) and non-bonding (5f $\delta_u$ and $\phi_u$) molecular orbitals,[64, 65] and for **2**-**4**, characteristic emission (four to five major vibronic peaks) was observed upon excitation at 420 nm (Figures S2, Supporting Information). Emission fine structure for compound **1** was not completely resolved at room temperature, thus a similar comment cannot be made for this material. The average vibronic progression of uranyl emission bands are coupled to the Raman active vibrational modes, and for **2**-**4** these values were found to match reasonably well with measured Raman frequencies highlighted in Figure 9 (Table S1, Supporting Information). Based on the values of the average vibronic gap between emission peaks, we can experimentally estimate the strength of the U-oxo bonds and the influence of the surrounding bonding. Lower values of the average vibronic gaps imply a stronger chemical interaction between the uranyl and Ag cations; however, this method seems to be more limited for gauging halogen bonding strengths. While we note the smallest average vibronic gap for **3**, which features our strongest CCI, per crystallographic metrics, these estimates indicate the halogen bonding in **2** is 'stronger' than the interactions in **4**. In contrast we note an average redshift of ca. 8 nm when qualitatively comparing the luminescence spectra of compounds **2** and **4**. We have demonstrated previously that equatorial ligand binding exerts greater influence on

resulting uranyl vibrational spectra in materials where there are halogen bonds with uranyl oxo atoms,[54] and here we suspect this behavior extends to photoluminescence spectra as well, due to small differences in $Ag^+$ equatorial coordination detailed in Figures 3 and 7.

**Computational Results**

In order to more comprehensively understand structural and spectroscopic findings for **1**-**4**, we turned to density functional theory (DFT) calculations and quantum theory of atoms in molecules (QTAIM) analysis to probe the results highlighted in previous sections. Initial DFT calculations were performed on a model system consisting of dimeric models of **1**-**4**, which were constructed using crystallographically-derived geometries. Partial optimization of the uranyl unit, all coordinating species, and the $Ag^+$ center was then performed, and these partially optimized structures were then analyzed to identify the symmetric ($\nu_1$) and asymmetric ($\nu_3$) uranyl stretching modes. Tables S3 and S4 (Supporting Information) contain the calculated values for $\nu_1$ and $\nu_3$, which broadly agree with experimental values with good quantitative accuracy, particularly for compounds **1**, **2**, and **4**. Notably, the significant decreases in $\nu_1$ and $\nu_3$ observed for **3** (Figures 9 and S3) are replicated, although some underestimation is noted for the calculated $\nu_3$ values.

To ascertain the specific role of the $Ag^+$ cations or iodine atoms with regards to potential 'charge transfer' to the uranyl oxo group and resulting spectroscopic effects, we first simplified the model of compound **1** to deconvolute the electronic interactions that impact uranyl vibrational spectra. This was done by starting with an optimized structure of, $[UO_2(C_7H_4IO_2)_2(NO_3)]^-$, which is a monomeric version compound **1** with the $Ag^+$ cation removed. This complex features $C_{2v}$ point group symmetry and U-oxo and U-$O_{eq}$ bond distances that are very similar to those described for compound **1**. Restoring the $Ag^+$ cation and then

calculating vibrational frequencies of the monomer, $[UO_2Ag(C_7H_4IO_2)_2(NO_3)]$, reveal a small influence of $Ag^+$ coordination at the uranyl oxo atoms as well, and support the idea that coordination of two benzoate oxygens reduces the delocalization of electron density into U - O π* orbitals. We also assessed the monomer via natural energy decomposition analysis (NEDA), which revealed a stabilization of 94.51 kcal/mol due to charge transfer interactions, with this value reflecting only the energy of interaction between $Ag^+$ with the iodo- and benzoate moieties of the monomer (Table S5, Supporting Information). Returning to analysis of compound **1**, we were unable to fully optimize geometries; however, NEDA reveals a stabilization of -120.55 kcal/mol per U=O/Ag unit due to charge transfer, i.e., 'covalent' interactions. To suggest that this interaction is the result only of the coordinate covalent bond between the uranyl oxo atom and the silver ion would be an oversimplification as NEDA only evaluates the changes in total energy arising from all of the interactions between fragments. With that said, it does provide a nice breakdown of the interactions into covalent (-241.115 kcal/mol), polarization (-258.795 kcal/mol), and electron pair repulsion (+405.094 kcal/mol), leading to a net stabilization of -94.816 kcal/mol for the dimer versus the calculated monomeric structure.

We also assessed compounds **1**-**4** using Natural Resonance Theory, via NBO, to further probe the ionic and covalent nature of halogen interactions and CCIs at the uranyl oxo atoms, which can be determined from first-order reduced density matrices, yielding properties such as Wiberg bond indices.[66] Via NBO analysis, and specifically Wiberg bond indices, one can extract metrical information, and for compound **1** we note a slightly lower bond order for the oxo atom (O2) that is coordinated to $Ag^+$ and a slightly increased U-O bond order for the terminal oxo group (Table S6, Supporting Information), which is likely due to the donation of electrons from the silver ion into U-oxo σ- or π-antibonding orbitals. In contrast to **1**, compound **2** includes $Ag^+$

coordination to only benzoate oxygens and aryl iodide groups, and here we note lower U-O bond orders for the bridging benzoate oxygens bound to $Ag^+$, when compared to non-bridging benzoate moieties (Table S7, Supporting Information). Uranyl oxo atoms participate in halogen bonding interactions in **2**; however, these do not impact the U-oxo bond order as much as in compound **1** where interactions were a result of a $UO_2$-Ag CCI. Compound **3** also features a $UO_2$-Ag CCI, similar to **1**, and NBO analysis shows many of the features identified above. Notably, the shorter $UO_2$-Ag CCI has an impact on resulting U-oxo bond orders as we see a clear weakening of U-oxo and U-O(benzoate) bonds due to $Ag^+$ coordination (Table S8, Supporting Information). Finally, in compound **4**, there is $Ag^+$ coordination only to benzoate oxygens and aryl iodide groups, similar to **2**, and interactions at the oxo atoms are bifurcated halogen bonds. The halogen interactions at the uranyl oxo atoms are some of the strongest that have been experimentally observed, yet NBO analysis finds that these interactions do not perturb the uranyl bonding directly (Table S9, Supporting Information). Moreover, this compound also affords the opportunity to compare uranyl centers with and without second sphere coordination of $Ag^+$, and in the former case we note weakening of U-O(benzoate) bond orders, in line with the results discussed above for **2**.

Compounds **1-4** were further evaluated via topological analysis using the Quantum Theory of Atoms in Molecules (QTAIM), where localized molecular orbitals were adapted from those derived from Natural Resonance Theory. For all four compounds, uranium charge and localization indices appear as expected for a U(VI) system. Values of the electron density at the bond critical point, $\rho_{BCP}$(U,O), and the delocalization index, δ(U,O), are also typical of the U-O interaction of uranyl, except for compound **3**, where the oxo atom directly coordinated by $Ag^+$ has a substantially lower $\rho_{BCP}$(U,O) and δ(U,O) (Table 3). Interestingly, the $UO_2$-Ag CCI in **1**

does not result in changes to bond critical points or delocalization indices of the same magnitude, which may reflect greater electron sharing in the $UO_2$-Ag interaction in **3**. Further comparison of each of the interactions at the uranyl oxo atoms in **1**-**4** (Table 3) demonstrates the substantial difference between $UO_2$-Ag CCIs and halogen bonding interactions. Bond critical points, $\rho_{BCP}$(Ag,O), and delocalization indices, δ(Ag,O), indicate a significant degree of electron sharing, which coupled with concomitant reductions in the same parameters for U-oxo interactions suggest that $UO_2$-Ag CCIs, particularly in compound **3**, are the origin of the reduction in vibrational frequencies (redshifts) highlighted in Figures 9 and S3 (Supporting Information), as well as Tables S3 and S4 (Supporting Information).

**Table 3** Topological parameters of uranyl cations as well as Ag-oxo CCIs (*) and I-O halogen bonding interactions ($^x$) in **1**-**4**. $\rho_{BCP}$ = magnitude of electron density at the bond or interaction critical point and δ(A,B) = delocalization index of the bond or non-covalent interaction.

| **Compound** | $\rho_{BCP}$(U,O) (a.u) | δ(U,O) | $\rho_{BCP}$(O, Ag) (a.u) | δ(O,Ag) | $\rho_{BCP}$(O, I) (a.u) |
|---|---|---|---|---|---|
| **1** | 0.325, 0.324*<br>0.325, 0.324* | 1.91, 1.83*<br>1.91, 1.83* | 0.034<br>0.034 | 0.214<br>0.214 | n/a |
| **2** | 0.309$^x$, 0.325<br>0.309$^x$, 0.325 | 1.87$^x$, 1.90<br>1.87$^x$, 1.88 | n/a | n/a | 0.008 |
| **3** | 0.306, 0.291<br>0.306, 0.285* | 1.86, 1.86<br>1.89, 1.73* | 0.045 | 0.291 | n/a |
| **4** | 0.323, 0.303<br>0.324, 0.301$^x$ | 1.90, 1.87<br>1.90, 1.81$^x$ | n/a | n/a | 0.0135<br>0.007 |

## Conclusions

The syntheses and crystal structures of four heterometallic compounds containing the $UO_2^{2+}$ cation, *o*- (**1**), *m*- (**2**), *p*-iodo- (**3**), and 2,5-diiodobenzoic acid (**4**) ligands, as well as $Ag^+$ cations are described and their means of covalent and supramolecular assembly have been detailed. Vibrational and luminescence spectra reveal redshifts with respect to the free uranyl

cation indicating that the CCIs and halogen-oxo interactions in **1**-**4** weaken U-oxo bonds, and in the case of compound **3** we note a rare example of activation of the uranyl asymmetric stretch ($\nu_3$) in the Raman spectra. Due to the engagement of the uranyl oxo atoms in each compound, this family of materials provides a platform to structurally and spectroscopically evaluate these two assembly motifs, which were quantifiably compared using quantum chemical calculations and density-based quantum theory of atoms in molecules (QTAIM) analysis. Both methods of theoretical analysis highlight a quantitative difference between halogen bonds and CCIs, with CCIs shown to significantly decrease uranyl bond orders and the electron density at the bond critical points, as well as significantly redshifting corresponding uranyl vibrational spectra. Halogen bonding interactions, on the other hand, are shown to have less influence, and in particular are noted to have limited impacts on uranyl vibrational spectra, which is consistent with previous computational and experimental studies.[54, 56] Collectively, the efforts described herein appreciably move forward our ongoing aims to enhance structure-property delineations in uranyl chemistry, particularly in complexes featuring oxo participation in covalent and non-covalent assembly. Future work is in-progress to expand the library of materials featuring oxo-based assembly motifs with the larger goal of developing experimental signatures and theoretical 'rules of the road' for systematic oxo atom participation, in both uranyl and transuranic systems.

**Supporting Information Available**

X-ray crystallographic files in CIF format, ORTEP figures of all compounds, IR, luminescence, and PXRD spectra of all compounds, tables of DFT and QTAIM results, and tables of selected bond lengths are all available. CIFs have also been deposited at the Cambridge Crystallographic Database Centre and may be obtained from http://www.ccdc.cam.ac.uk by citing reference numbers 2038396-2038399 for compounds **1**-**4**, respectively.

**Author Information**

Corresponding Author

*E-mail: cahill@gwu.edu Phone: (202) 994-6959

**Notes**

The authors declare no competing interests.

**Acknowledgements**

This study was supported by the U.S. Department of Energy (DOE)—Chemical Sciences, Geosciences and Biosciences Division, Office of Science, Office of Basic Energy Sciences, Heavy Elements Program, under grant number DE-FG02-05ER15736. The authors would also like to thank the Center for Sustainable Energy at Notre Dame University (ND Energy) for Infrared spectrometer and Raman microscope time. We also thank Dr. Mirjana Dimitrievska of the National Institutes of Standards and Technology (NIST) and Dr. Richard Wilson of Argonne National Laboratory for valuable discussions related to Raman spectroscopy. M.K. is currently supported by the Department of Defense (DoD) through the National Defense Science and Engineering Graduate (NDSEG) Fellowship Program and is the recipient of an Achievement Rewards for College Scientists (ARCS) Foundation Fellowship at the University of California San Diego.

**References**

1. C. L. Cahill, D. T. de Lill and M. Frisch, *CrystEngComm*, 2007, **9**, 15-26.
2. K.-X. Wang and J.-S. Chen, *Accounts of Chemical Research*, 2011, **44**, 531-540.
3. M. B. Andrews and C. L. Cahill, *Chemical Reviews*, 2013, **113**, 1121-1136.
4. T. Loiseau, I. Mihalcea, N. Henry and C. Volkringer, *Coordination Chemistry Reviews*, 2014, **266–267**, 69-109.
5. W. Yang, T. G. Parker and Z.-M. Sun, *Coordination Chemistry Reviews*, 2015, **303**, 86-109.
6. R. G. Surbella III and C. L. Cahill, in *Handbook on the Physics and Chemistry of Rare Earths*, eds. J.-C. G. Bünzli and V. K. Pecharsky, Elsevier, Amsterdam, 2015, vol. 48, ch. 276, pp. 163-285.

7. A. S. Jayasinghe, M. K. Payne and T. Z. Forbes, *Journal of Solid State Chemistry*, 2017, **254**, 25-31.
8. J. Xie, Y. Wang, M. A. Silver, W. Liu, T. Duan, X. Yin, L. Chen, J. Diwu, Z. Chai and S. Wang, *Inorganic Chemistry*, 2018, **57**, 575-582.
9. E. A. Dolgopolova, A. M. Rice and N. B. Shustova, *Chemical Communications*, 2018, **54**, 6472-6483.
10. S. Schöne, T. Radoske, J. März, T. Stumpf and A. Ikeda-Ohno, *Inorganic Chemistry*, 2018, **57**, 13318-13329.
11. P. Harvey, A. Nonat, C. Platas-Iglesias, L. S. Natrajan and L. J. Charbonnière, *Angewandte Chemie International Edition*, 2018, **57**, 9921-9924.
12. G. E. Gomez, J. A. Ridenour, N. M. Byrne, A. P. Shevchenko and C. L. Cahill, *Inorganic Chemistry*, 2019, **58**, 7243-7254.
13. P. Thuery and J. Harrowfield, *Dalton Transactions*, 2017, **46**, 13660-13667.
14. K. P. Carter, A. T. Kerr, I. V. Taydakov and C. L. Cahill, *Solid State Sciences*, 2018, **76**, 20-32.
15. K. P. Carter, M. Kalaj and C. L. Cahill, *Inorganic Chemistry Frontiers*, 2017, **4**, 65-78.
16. K. P. Carter, M. Kalaj, R. G. Surbella III, L. C. Ducati, J. Autschbach and C. L. Cahill, *Chemistry – A European Journal*, 2017, **23**, 15355-15369.
17. K. P. Carter, M. Kalaj, A. Kerridge, J. A. Ridenour and C. L. Cahill, *Inorganic Chemistry*, 2018, **57**, 2714-2723.
18. K. P. Carter, R. G. Surbella III, M. Kalaj and C. L. Cahill, *Chemistry – A European Journal*, 2018, **24**, 12747-12756.
19. J. A. Ridenour, M. H. Schofield and C. L. Cahill, *Crystal Growth & Design*, 2020, **20**, 1311-1318.
20. P. Thuéry and J. Harrowfield, *Inorganic Chemistry*, 2016, **55**, 6799-6816.
21. L. Mei, K.-Q. Hu, Z.-H. Zhang, S.-Q. An, Z.-F. Chai and W.-Q. Shi, *Inorganic Chemistry*, 2018, **57**, 4673-4685.
22. Z.-T. Yu, Z.-L. Liao, Y.-S. Jiang, G.-H. Li and J.-S. Chen, *Chemistry – A European Journal*, 2005, **11**, 2642-2650.
23. F. Wang, F.-L. Li, M.-M. Xu, H. Yu, J.-G. Zhang, H.-T. Xia and J.-P. Lang, *Journal of Materials Chemistry A*, 2015, **3**, 5908-5916.
24. C. W. Abney, Y. Nan and L. L. Tavlarides, *Industrial & Engineering Chemistry Research*, 2017, **56**, 4837-4846.
25. D. Banerjee, X. Chen, S. S. Lobanov, A. M. Plonka, X. Chan, J. A. Daly, T. Kim, P. K. Thallapally and J. B. Parise, *ACS Applied Materials & Interfaces*, 2018, **10**, 10622-10626.
26. M. Kalaj, K. P. Carter, A. V. Savchenkov, M. M. Pyrch and C. L. Cahill, *Inorganic Chemistry*, 2017, **56**, 9156-9168.
27. *SAINT*, Bruker AXS Inc. Madison, Wisconsin, USA, 2007.
28. *APEXII*, Bruker AXS Inc. Madison, Wisconsin, USA, 2008.
29. L. Krause, R. Herbst-Irmer, G. M. Sheldrick and D. Stalke, *Journal of Applied Crystallography*, 2015, **48**, 3-10.
30. *TWINABS*, Bruker AXS Inc. Madison, Wisconsin, USA, 2008.
31. G. Sheldrick, *Acta Crystallographica Section C*, 2015, **71**, 3-8.
32. A. Altomare, G. Cascarano, C. Giacovazzo, A. Guagliardi, M. C. Burla, G. Polidori and M. Camalli, *Journal of Applied Crystallography*, 1994, **27**, 435-435.

33. L. Farrugia, *Journal of Applied Crystallography*, 2012, **45**, 849-854.
34. *CrystalMaker*, Crystal Maker Software Limited, Bicester, England, 2009.
35. H. Putz and K. Brandenburg, *Match! - Phase Identification from Powder Diffraction*, Crystal Impact, Bonn, Germany, 2015.
36. P. Di Pietro and A. Kerridge, *Inorganic Chemistry*, 2016, **55**, 573-583.
37. P. Di Pietro and A. Kerridge, *Physical Chemistry Chemical Physics*, 2016, **18**, 16830-16839.
38. T. H. Dunning Jr., *The Journal of Chemical Physics*, 1989, **90**, 1007-1023.
39. F. Weigend and R. Ahlrichs, *Physical Chemistry Chemical Physics*, 2005, **7**, 3297-3305.
40. W. Küchle, M. Dolg, H. Stoll and H. Preuss, *The Journal of Chemical Physics*, 1994, **100**, 7535-7542.
41. X. Cao, M. Dolg and H. Stoll, *The Journal of Chemical Physics*, 2003, **118**, 487-496.
42. X. Cao and M. Dolg, *Journal of Molecular Structure: THEOCHEM*, 2004, **673**, 203-209.
43. D. Andrae, U. Häußermann, M. Dolg, H. Stoll and H. Preuß, *Theoretica Chimica Acta*, 1990, **77**, 123-141.
44. A. Bergner, M. Dolg, W. Küchle, H. Stoll and H. Preuß, *Molecular Physics*, 1993, **80**, 1431-1441.
45. R. Ahlrichs, M. Bär, M. Häser, H. Horn and C. Kölmel, *Chemical Physics Letters*, 1989, **162**, 165-169.
46. M. J. Frisch, G. W. Trucks, H. B. Schlegel, G. E. Scuseria, M. A. Robb, J. R. Cheeseman, G. Scalmani, V. Barone, G. A. Petersson, H. Nakatsuji, X. Li, M. Caricato, A. Marenich, J. Bloino, B. G. Janesko, R. Gomperts, B. Mennucci, H. P. Hratchian, J. V. Ortiz, A. F. Izmaylov, J. L. Sonnenberg, D. Williams-Young, F. Ding, F. Lipparini, F. Egidi, J. Goings, B. Peng, A. Petrone, T. Henderson, D. Ranasinghe, V. G. Zakrzewski, J. Gao, N. Rega, G. Zheng, W. Liang, M. Hada, J. A. Montgomery, J. E. Peralta, F. Ogliaro, M. Bearpark, J. J. Heyd, E. Brothers, K. N. Kudin, V. N. Staroverov, T. Keith, R. Kobayashi, J. Normand, K. Raghavachari, A. Rendell, J. C. Burant, S. S. Iyengar, J. Tomasi, M. Cossi, J. M. Millam, M. Klene, C. Adamo, R. Cammi, J. W. Ochterski, R. L. Martin, K. Morokuma, O. Farkas, J. B. Foresman and D. J. Fox, *Gaussian 16*, *Revision C.*01, Gaussian, Inc., Wallingford, Connecticut, USA, 2016.
47. E. D. Glendening, J. K. Badenhoop, A. E. Reed, J. E. Carpenter, J. A. Bohmann, C. M. Morales, P. Karafiloglou, C. R. Landis and F. Weinhold, *NBO 7.0*, Theoretical Chemistry Institute, University of Wisconsin, Madison, Wisconsin, USA, 2018.
48. J. P. Foster and F. Weinhold, *Journal of the American Chemical Society*, 1980, **102**, 7211-7218.
49. T. A. Keith, *AIMA11*, version 19.10.12, TK Gristmall Software, Overland Park, Kansas, USA, 2019.
50. R. F. W. Bader, *Atoms in Molecules: A Quantum Theory*, Oxford University Press, Oxford, UK, 1990.
51. R. Dennington, T. A. Keith and J. M. Millam, *GaussView 6*, Semichem Inc., Shawnee Mission, Kansas, USA, 2019.
52. M. D. Hanwell, D. E. Curtis, D. C. Lonie, T. Vandermeersch, E. Zurek and G. R. Hutchison, *Journal of Cheminformatics*, 2012, **4**, 17.
53. P. Thuéry and J. Harrowfield, *Crystal Growth & Design*, 2017, **17**, 2116-2130.
54. M. Kalaj, K. P. Carter and C. L. Cahill, *European Journal of Inorganic Chemistry*, 2017, **2017**, 4702-4713.

55. M. Kalaj, K. P. Carter and C. L. Cahill, *Acta Crystallographica Section B*, 2017, **73**, 234-239.
56. K. P. Carter, M. Kalaj, A. Kerridge and C. L. Cahill, *CrystEngComm*, 2018, **20**, 4916-4925.
57. A. Kerridge, *Chemical Communications*, 2017, **53**, 6685-6695.
58. G. Lu, A. J. Haes and T. Z. Forbes, *Coordination Chemistry Reviews*, 2018, **374**, 314-344.
59. G. Herzberg, *Infrared and Raman Spectra of Polyatomic Molecules*, D. Van Nostrand Company, Inc., New York, NY, 1946.
60. K. Nakamoto, *Infrared and Raman Spectra of Inorganic and Coordination Compounds Part A: Theory and Applications in Inorganic Chemistry*, John Wiley & Sons, Inc., New York, NY, 5th edn., 1997.
61. J. A. Platts and R. J. Baker, *Physical Chemistry Chemical Physics*, 2018, **20**, 15380-15388.
62. R. M. Badger, *The Journal of Chemical Physics*, 1935, **3**, 710-714.
63. J. Cioslowski, G. Liu and R. A. Mosquera Castro, *Chemical Physics Letters*, 2000, **331**, 497-501.
64. R. G. Denning, *The Journal of Physical Chemistry A*, 2007, **111**, 4125-4143.
65. L. S. Natrajan, *Coordination Chemistry Reviews*, 2012, **256**, 1583-1603.
66. K. B. Wiberg, *Tetrahedron*, 1968, **24**, 1083-1096.